scientific reports

OPEN

Research on the mechanism of fault sliding casing damage under the effect of water immersion deterioration of rock mass

Yaosheng Zhang[1,2], Yu Shao[1,2], Decai Mi[1,2], Biao Wang[3✉] & Yi Li[4]

Hydraulic fracturing-induced casing deformation has garnered significant attention, yet the effects of water immersion-induced rock deterioration remain underexplored. This study employs finite element analysis to investigate casing shear deformation in fault-sliding scenarios under water immersion deterioration. A 3D casing cement sheath-formation system model with varying water immersion parameters was developed to analyze casing mechanical properties and deformation. Results indicate that an 80% reduction in cohesion increases casing Mises stress by approximately fourfold, significantly impacting casing forces. A 60% reduction in the internal friction angle raises Mises stress by about 20%, exerting a weaker influence compared to cohesion changes. Decreasing the fault sliding surface friction coefficient elevates both Mises stress and inner diameter deformation; a reduction from 0.7 to 0.1 more than doubles Mises stress and increases resistance length eightfold. This study offers insights for designing casing damage models considering rock water immersion, optimizing fracturing parameters, and determining bridge plug dimensions.

Keywords Water immersion deterioration, Fault slip, Casing deformation, Numerical simulation, Cohesion, Internal friction angle, Friction coefficient

According to the forecast report of the International Energy Agency, at least until the middle of the twenty-first century, oil and gas resources are still the main energy for global development[1]. However, as the world attaches great importance to unconventional oil and gas resources and invests a lot of manpower and material resources in development, wellbore safety, and casing-cement sheath-formation system (CCFS) deformation have become issues of safe production that need to be studied urgently, which is of great significance for improving the economic benefits and environmental protection of unconventional oil and gas production[2]. As a key component of oil and gas wells, casing provides the main mechanical structural barrier for oil and gas wells and is also a pipeline in oil and gas production during its life cycle[3]. Wellbore integrity research involves mechanical problems, including but not limited to geomechanics, rock mechanics, structural mechanics, fluid mechanics, elastic–plastic mechanics, and thermodynamics. Therefore, there are many factors that cause casing failure, and the coupling mechanism is very complicated. Unlike traditional shale gas production, unconventional shale gas production often requires multiple stages of fracturing to improve production efficiency. Multi-stage fracturing also causes casing deformation while increasing production. The fracturing process can cause pore pressure changes, stress redistribution, fault activation, and microseismic events[4,5]. King et al.[6] proposed that multi-stage fracturing should be alert to the increase in casing load, and protective measures should be taken for oil and gas wells with risk of failure to ensure safety.

So far, scholars have done a lot of research on the effects of wellbore load forms, geological factors, and engineering factors on casing. Atkinson et al.[7] performed in-plane and out-of-plane analyses of casing internal loads, external loads, and bond stresses. Yin et al.[8] established a casing mechanics model for directional wells according to the trajectory and in-situ stress of oil and gas wells. Fang et al.[9] established an analytical model of multi-layer composite casing considering various formations and studied the collapse strength of casing. Gao et al.[10] and Tan et al.[11] believed that the casing wear should be considered during the running process of the drilling

[1]Guangxi Beibu Gulf Investment Group Co., Ltd, Nanning 530022, China. [2]Guangxi Communications Design Group Co., Ltd, Nanning 530022, China. [3]State Key Laboratory of Deep Metal Mining and Equipment, Northeastern University, Shenyang 110819, China. [4]Department of Engineering Geology, Institute of Applied Geosciences, Technical University of Berlin, Ernst-Reuter-Platz 1, BH 3-1, 10587 Berlin, Germany. ✉email: Billwang1114@163.com

tool, and studied the wear of the casing's inner wall and proposed a prediction model. Affected by the cementing quality, the eccentric behavior of casing and cement sheath, cement annulus[12], and sustained casing pressure[13] have also received attention and have been studied. Liang et al.[14,15] studied the deformation and stability of oil and gas wells under longwall gas co-production. The above studies provide theoretical guidance for the safe exploitation of shale gas resources.

Existing studies attribute the main factors of casing failure to the effects of non-uniform in-situ stress, rock fracture propagation, and fault slip. Among them, it has become a consensus that casing shear failure is the main failure mode of casing[16–18], and the shear deformation of casing is closely related to the fault slip caused by multi-stage fracturing[19]. Research indicates that fault slip can trigger earthquakes and associated deformations, posing significant threats to underground structures[20–22]. Meng et al.[23] and Xi et al.[24] analyzed the influencing factors such as fault strike angle, slip distance, and formation mechanical properties. However, in the process of hydraulic fracturing, scholars have paid more attention to the expansion of rock mass cracks and the deterioration of rock mass strength caused by fracturing. For example, Feng et al.[25,26] used the finite element method to study the stress near the wellbore and the generation and propagation law of cracks around the wellbore, and believed that the initial defect at the interface of the composite body can significantly reduce the pressure transfer, and concluded that the wellbore The law that makes cracks develop vertically at the cemented surface[27–30]; Moradian et al.[31] proved through rock direct shear experiments that when the effective normal stress is low, small slip events on the rough surface will cause shear dilatation, resulting in a significant increase in the pore diameter of rock fractures; the above research has an understanding of the failure mechanism of casing goes deeper, but ignores the quantitative relationship between rock mass degradation and changes in casing performance. As shown in Fig. 1, the hydraulic fracturing technology not only changes the stress state of the rock mass while increasing production but also causes the water immersion deterioration of the rock around the well. According to the Mohr–Coulomb criterion, water injection increases the shear stress while reducing the normal stress, which could trigger fault slip. Moreover, water erosion leads to a decrease in the cohesion and internal friction angle of the rock mass, exacerbating the deterioration of rock strength and intensifying fault slip behavior. The above phenomena significantly affect the mechanical and deformation characteristics of the casing-cement sheath-strata system, thereby increasing the risk of casing failure. The casing loss rate of most water injection wells is significantly higher than that of production wells. Therefore, the study of the stress and deformation characteristics of the casing under the rock mass degradation can have a clearer understanding of the failure mechanism of the rock mass in different states, and provide a reference for the design of preventing casing damage. It is of great significance to study the mechanism of fault sliding casing damage.
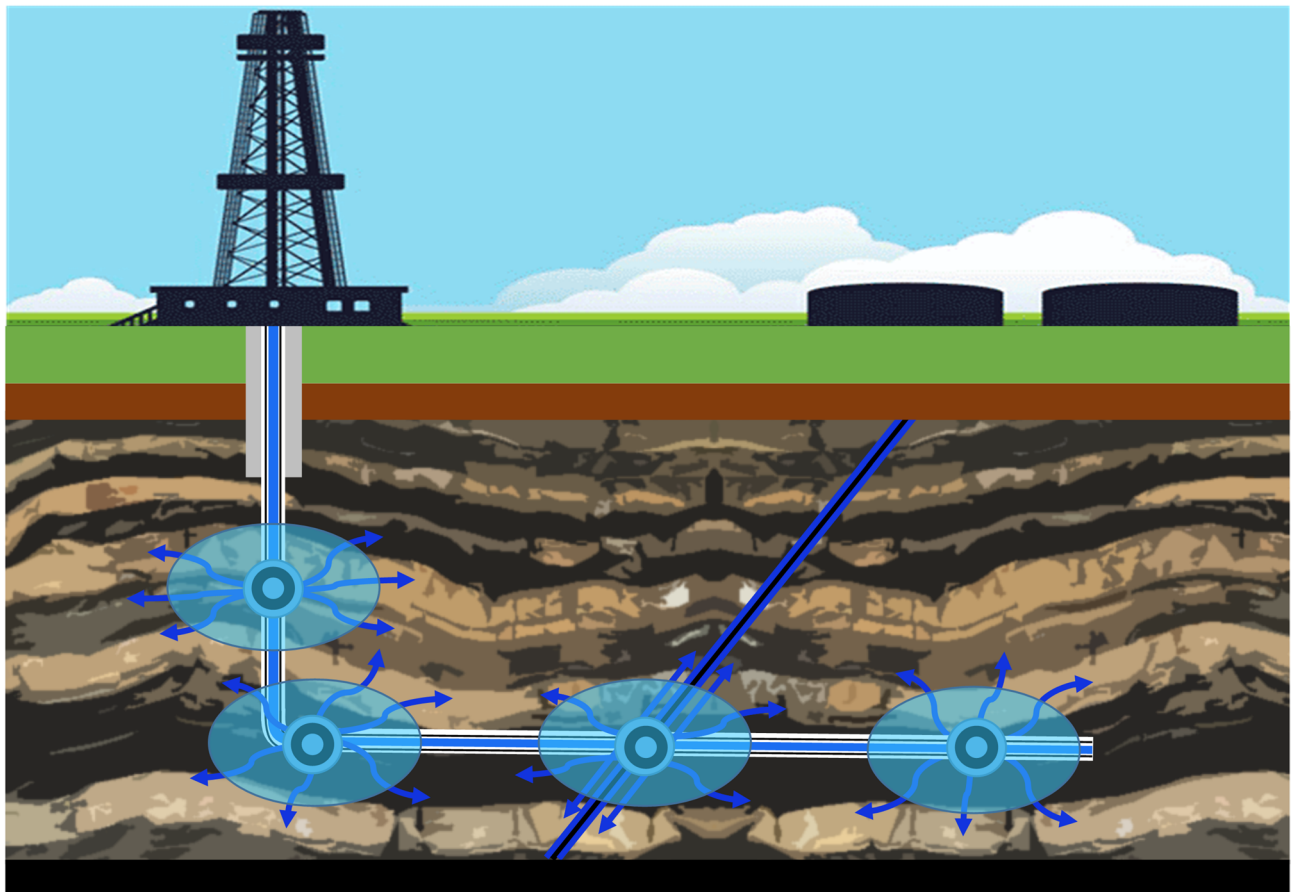

Fig. 1. Schematic diagram of water immersion of rock mass and sliding surface.

This study investigates the mechanism of fault sliding-induced casing failure under water immersion degradation, utilizing a finite element model validated by logging data and comparing theoretical and numerical solutions. The effects of varying water immersion degradation levels, fault plane friction coefficients, and effective stresses on casing behavior were analyzed parametrically. The relationship between casing stress and deformation under water immersion-induced rock mass deterioration was established. This research provides a foundation for designing casing damage models considering rock water immersion, optimizing fracturing parameters, and determining bridge plug dimensions.

Calculation of casing deformation of fault slip type

Stress analysis of CCFS system

Perform force analysis on CCFS, as shown in Fig. 2, all forces can be simplified into axial, radial stresses, assuming that D_a, D_b, D_c are the inner and outer radius of the casing and the outer radius of the cement sheath, are the elastic modulus of the casing and cement sheath, are the Poisson's ratio of the casing and cement sheath, are the internal pressure, the external extrusion force of the casing and cement sheath, and the pressure at the interface between casing and cement sheath, the weight of the casing material is γ, and the total length of the casing is L. If a polar coordinate system is established at the wellhead, The stress in the three directions can be expressed by Eqs. (1), (2), and (3):

$$\sigma_r = \frac{D_a^2}{D_b^2 - D_a^2}\left(1 - \frac{D_b^2}{r^2}\right)P_i - \frac{D_b^2}{D_b^2 - D_a^2}\left(1 - \frac{D_a^2}{r^2}\right)P_e \tag{1}$$

$$\sigma_\theta = \frac{D_a^2}{D_b^2 - D_a^2}\left(1 + \frac{D_b^2}{r^2}\right)P_i - \frac{D_b^2}{D_b^2 - D_a^2}\left(1 + \frac{D_a^2}{r^2}\right)P_e \tag{2}$$

$$\sigma_z = \frac{2\nu}{D_b^2 - D_a^2}\left(D_a^2 P_i - D_b^2 P_e\right) + \gamma\left(L - Z\right) \tag{3}$$

Based on the derivation process of Equations A1 to A23 in Appendix A., the collapse strength of casing under the combination of casing and cement sheath can be obtained as shown in Eq. (4):

$$P_m = \frac{D_a^2 - D_b^2}{2D_b^2} \cdot \frac{Y_P}{K} \tag{4}$$

Fault slip condition

Mohr–Coulomb criterion and effective stress principle can judge whether the fault slips. According to Eqs. (5) and (6), it can be determined that when the pressure of fracturing fluid increases to a certain value, the shear
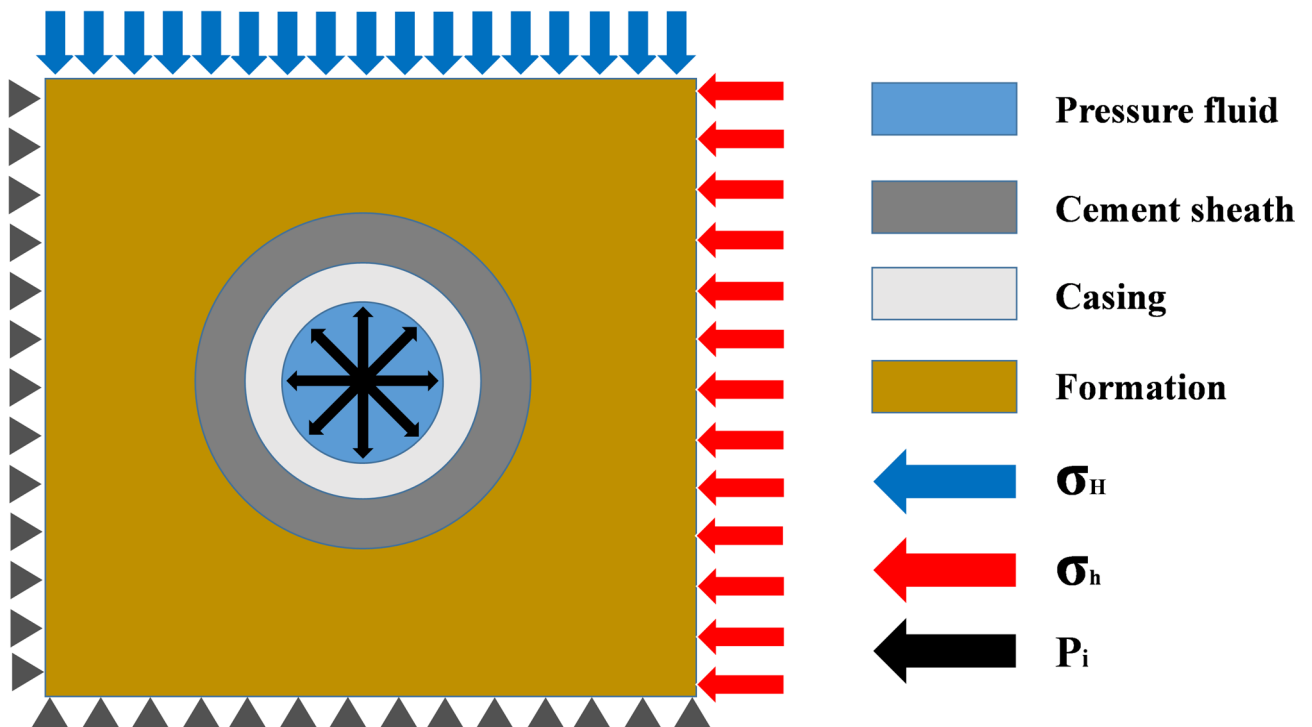

Fig. 2. CCFS system stress analysis.

stress of the fault plane will exceed the pore pressure, resulting in fault slip. Equation (7) is the critical pore pressure value of fault strike-slip. Microseismic monitoring technology can better capture the sliding of unstable faults and can judge the magnitude and fault location according to the characteristics of microseismic signals monitored on-site[32].

$$\tau > \mu \sigma_E + C \tag{5}$$

where:

τ Refers to the shear stress of the fault plane, MPa; μ refers to the friction coefficient; σ_E refers to the effective stress, MPa; C refers to the cohesion of rock, MPa.

$$\sigma_E = \sigma_n - P \tag{6}$$

where:

σ_n Refers to the normal stress of fracture surface, MPa; P refers to the pore pressure, MPa.

$$P = \frac{C}{\mu} + \sigma_3 + (\sigma_1 - \sigma_3)\left(\sin^2\phi - \frac{\sin\phi\cos\phi}{\mu}\right) \tag{7}$$

where:

σ_1 Refers to the maximum principal stress, MPa; σ_3 refers to the minimum principal stress, MPa; ϕ refers to the angle between the fault plane and the maximum principal stress.

Calculation of earthquake-induced fault slip distance

T. C. Hanks et al.[33] defined the relationship between moment magnitude and seismic moment, as shown in the Eq. (8).

$$M_W = \frac{2}{3}(\lg M_0 - 9.1) \tag{8}$$

where:

M_W Represents the moment magnitude; M_0 represents the seismic moment.

According to the different earthquake scales, the fault plane can be represented by a rectangle and a circle. Large earthquakes are usually represented by rectangular sections, while small earthquakes are more suitable to be represented by circular sections[34]. The relationship between fault size, slip distance, moment magnitude, and stress drop can be expressed by Eqs. (9) and (10).

$$r = \sqrt[3]{\frac{7 \times 10^{1.5M_W+9.1}}{16\Delta\sigma}} \tag{9}$$

$$L = \frac{16\Delta\sigma r}{7\pi G} \tag{10}$$

where:

r Represents the fault radius, m; $\Delta\sigma$ represents the magnitude of fault stress drop caused by an earthquake, MPa; D represents the sliding distance, mm; G represents the fault stiffness, GPA.

Mukuhira[19,35] shows through statistical data that the stress drop range generated by most microseismic events is distributed in the range of 0.1 ~ 1 MPa. According to (9) and (10), the sliding distance of the fault can be calculated, and then the peak value of shear displacement can be calculated according to Eq. (11). The deformation of the casing can be approximately expressed by Eq. (12).

$$u = \frac{\tau}{K_s} \tag{11}$$

where:

u Represents the peak value of shear displacement, mm; K_s represents the shear stiffness of the fault, GPA.

$$\Delta D = L - u \tag{12}$$

Method
Materials parameters

The 3D finite element analysis of CCFS was carried out with software ABAQUS. In order to understand the deformation and failure mechanism of the casing more accurately, the material properties were set based on the following criteria. As shown in Fig. 3, the casing was set as an ideal elastic–plastic constitutive model, and the cement sheath was set as CDP (concrete damage plastic model) concrete plastic damage model, the rock formation was set to the Mohr–Coulomb elastic–plastic constitutive model. The model uses P110 steel grade casing, C30 grade concrete, and formation parameters from laboratory tests, detailed parameters are presented in Table 1.
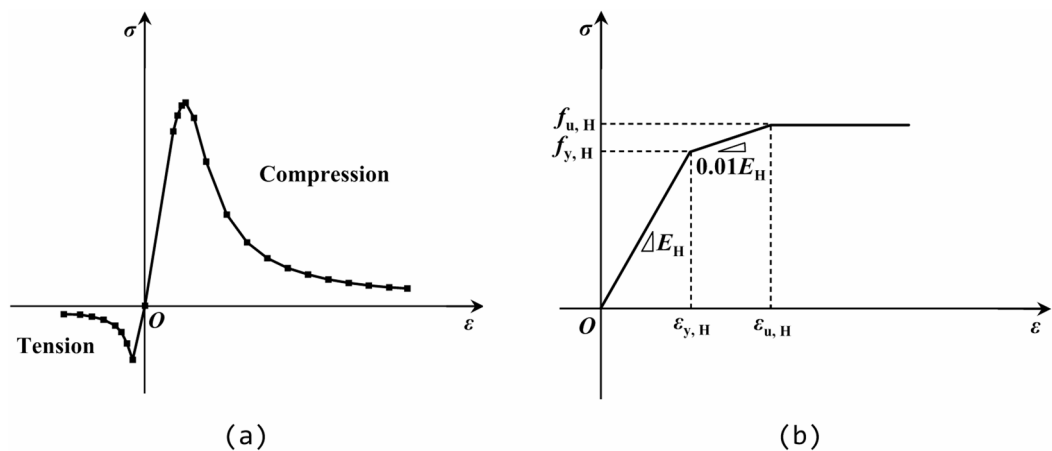
Fig. 3. Schematic diagram of constitutive model. (**a**) Concrete damage plasticity model. (**b**) Ideal elastic-plastic model.

Material	Elastic modulus E/GPa	Poisson's ratio μ	Yield strength σ_s/MPa	Cohesion C/MPa	Friction angle Ψ/°
Casing	210	0.3	758	/	/
Cement sheath	10	0.17	30	/	/
Dark grey mudstone 1	2.53	0.282	/	36.02	15.44
Black gray mudstone 1	2.827	0.16	/	37.16	13.495
Brown-black oil shale 1	4.749	0.156	/	35.64	18.74
Grey oil-stained argillaceous sandstone 1	3.748	0.216	/	37.05	22.398
Dark grey mudstone 2	3.47	0.113	/	20.15	13.078
Gray powder mud with oil stains	2.08	0.205	/	24.12	12.678
Gray oil spotted powder mud sandstone	2.272	0.19	/	24.18	13.613
Black gray mudstone 2	2.362	0.185	/	25.16	13.24
Gray green mudstone 1	2.374	0.18	/	24.98	14.052
Brown-black oil shale 2	2.398	0.162	/	25.24	13.56
Gray black mudstone 1	2.576	0.173	/	24.06	13.1
Grey oil-stained argillaceous sandstone 2	2.360	0.2	/	35.63	16.2
Silty mudstone with oil stains	2.369	0.26	/	39.12	26.33
Gray black mudstone 2	2.987	0.24	/	31.04	30.2
Gray green mudstone 2	2.436	0.27	/	29.84	25.47

Table 1. Mechanical parameters.

Boundary conditions, meshing, and contact elements
Basic assumptions

- The single-material rock formation, cement sheath, and casing all satisfy the homogeneity and isotropy assumptions;
- The cement sheath and casing are regarded as a thin and uniform cylinder, and their initial defects are ignored;
- The model adopts the finite element method for calculation, and the calculation element satisfies the assumption of small displacement and small deformation.

Grids and contacts

The model parameters are taken from a certain oil and gas well project with a burial depth of 2800 m. The model shown sets three load conditions and one displacement condition, in which the vertical in-situ stress, the horizontal in-situ stress and the fluid pressure in the pipeline are all from the field monitoring data. The specific boundary conditions and element settings are as follows:

- Acting on the upper part of the model to simulate vertical in-situ stress; (Vertical in-situ stress: 54 MPa)
- Acting on the four sides of the model to simulate the horizontal in-situ stress; (Maximum horizontal ground stress: 20 MPa, minimum horizontal ground stress: 17 MPa)

- Acting on the inside of the casing to simulate the fluid pressure in the pipeline; (Fluid pressure in pipe: 10 MPa)
- The bottom surface is set as a fully fixed constraint;
- Select the C3D8R unit for mesh division;
- The way of interaction between contact elements, the tangential behavior is set to the friction coefficient through the penalty function, and the normal behavior is set to hard contact.

Judgment of casing shear failure caused by fault slip

In this paper, the failure of the casing is judged by the yield of the casing and the resistance of the drill pipe (or the lower set of tools):

Casing yield
As a metal material, it is appropriate to use the Von Mises criterion to determine the yield of the casing. The Von Mises yield criterion is that the equivalent stress is always equal to the flow stress in the plastic state, and the yield function is shown in Eq. (13).

$$f\left(\sigma_1, \sigma_2, \sigma_3\right) = \frac{1}{\sqrt{2}} \sqrt{\left(\sigma_1 - \sigma_2\right)^2 + \left(\sigma_2 - \sigma_3\right)^2 + \left(\sigma_3 - \sigma_1\right)^2} \tag{13}$$

Stuck drill pipe
The drill pipe and deformed casing are shown in Fig. 4, if the casing is greatly deformed, resulting in the obstruction of the passage of the drill pipe, the minimum inner diameter of the deformed casing and the diameter of the drill pipe can be judged by Eq. (14). If the minimum inner diameter of the casing is less than the diameter of the drill pipe, the casing is considered to be invalid.

$$D_d \geq D_c \tag{14}$$

where:
D_d represents the diameter of drill pipe, mm; D_c represents the maximum inner diameter of casing, mm.

Method reliability verification

The geometric size of the model is selected as 2 m in length, 2 m in width and 4.75 m in height. The model includes 32 rock formations of 9 different lithologies except for casing and cement sheath. The distribution is shown in Fig. 5, The outer diameter of the caing is 139.7 mm and the thickness is 7.72 mm; The outer diameter of the cement sheath is 225 mm and the thickness is 42.65 mm. The specific mechanical parameters are shown in Table 1.

It can be clearly seen from Fig. 6 that the stress characteristics of the formations are distributed in layers, the larger deformation and failure positions are concentrated near the wellbore, there are many damage areas in the surrounding rock of the wellbore, and the damage areas are distributed at the interface of formations with
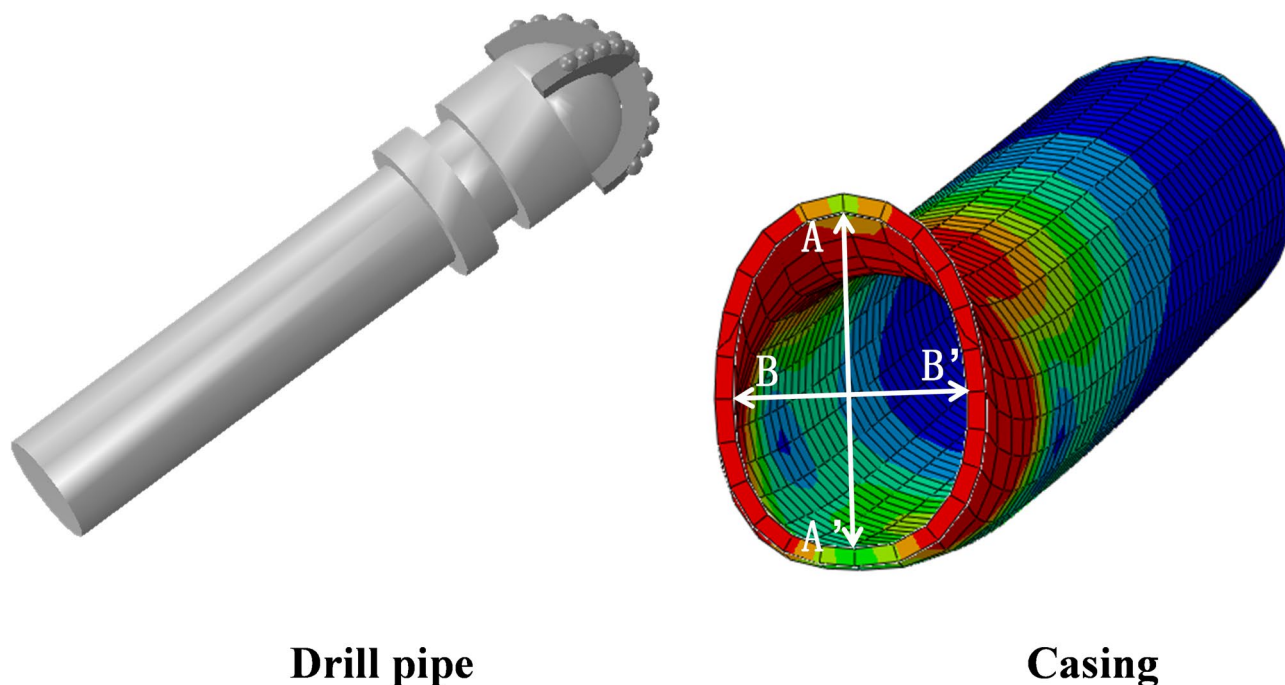

Drill pipe   Casing

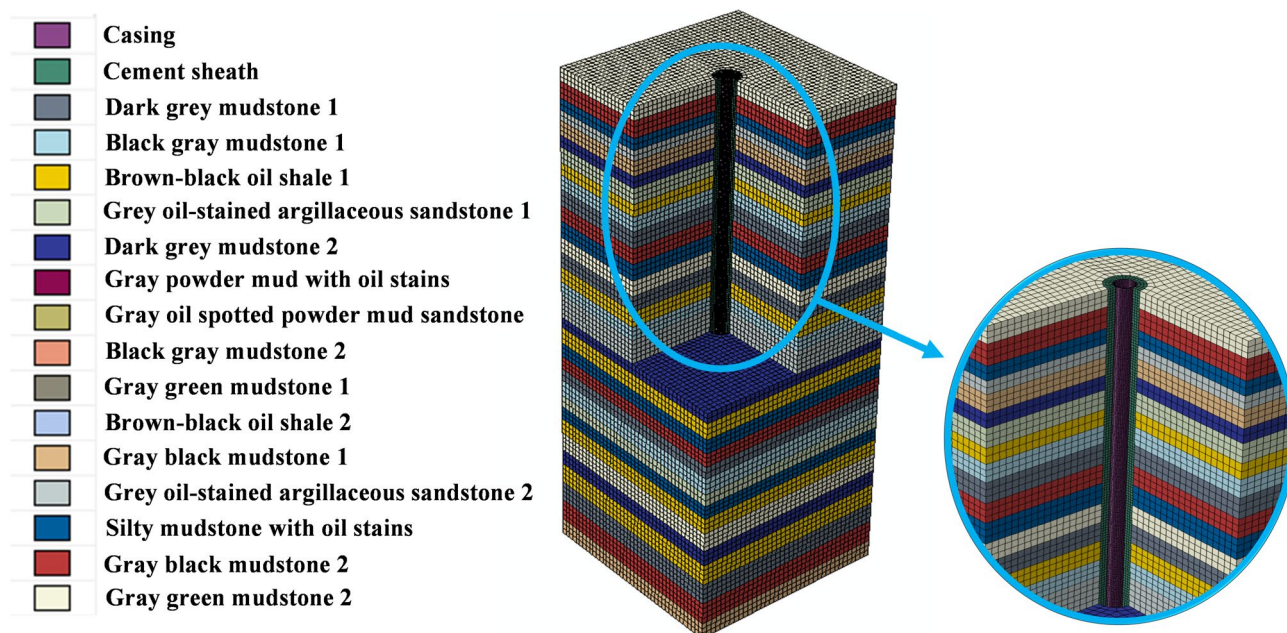**Fig. 4**. Schematic diagram of drill pipe encountering resistance.

Fig. 5. model diagram.

different lithologies. The deformation of the surrounding rock of the wellbore is mainly shear and extrusion deformation, which is basically consistent with the logging data and the rock damage characteristics in the field. The feasibility of the research method is also demonstrated, and the necessity of carrying out formation sliding research is also demonstrated.

Fault-slip-type CCFS model for rock mass degradation caused by water immersion
Model parameters
In order to weaken the interference of other factors, a simpler fault slip model as shown in Fig. 7 was established for research, and the lithology of the stratum was selected, and the lithology of the stratum where the casing fault occurred in a site—brown-black oil shale was selected. The material properties, boundary conditions and basic assumptions of the model are given in part 3.1–3.2. The calculation unit is shown in Table 2.

Working condition setting
In this paper, the mechanical parameters of the brown-black oil shale 1 in part 3.2 are selected. The uniaxial compressive strength tests on the brown-black oil shale samples after soaking indicate that the elastic modulus decreased by approximately 2.0 GPa, cohesion dropped by about 80%, and the internal friction angle decreased by around 60%. Based on these findings, we have adjusted the strength parameters in the CCFS mechanical model accordingly. The variation range of the parameters is shown in Table 3.

Result analysis
The stress distribution calculated by the model is shown in Fig. 8. The casing and cement sheath yield failure near the sliding surface, and the maximum deformation position is not at the intersection with the sliding surface, but near the sliding surface 100–200 mm, Fig. 9a shows the plastic zone distribution of the casing and cement sheath when the fault slip distance is 60 mm, and Fig. 9b shows the plastic zone distribution of the hanging wall and footwall strata during the fault sliding process. The length of the plastic zone is about 200 mm.

Figure 10 shows the theoretical calculation results obtained according to Eq. (12) (the fault peak value of shear displacement was selected 2.8 mm[36]), the calculation results of this model, the results of Zhang F et al. and the results of Zhang X et al. The results show that the reduction of casing inner diameter theoretically calculated is in direct proportion to the slip distance, while the results of finite element calculation are nonlinear. When the slip distance is less than 15 mm, the theoretical value is close to the results of finite element calculation, When the sliding distance is greater than 15 mm, the difference between the two gradually increases. This phenomenon is caused by the failure of the rock element calculated by the finite element method, which is not considered in the theoretical calculation.

Figures 11 and 12 show the circumferential and radial stresses at the locations of the casing and cement sheath plastic zones, respectively. Both the circumferential stress and radial stress of the casing and cement sheath change with the angle. The results show that the circumferential stress and radial stress of the casing perpendicular to the sliding direction of the fault increase significantly, and the maximum circumferential stress reaches 156.496 MPa, which exceeds the outer extrusion strength of the casing, the maximum radial compressive stress reaches 740.653 MPa, the maximum radial tensile stress reaches 515.124 MPa; the maximum circumferential stress of the cement sheath reaches 37.295 MPa, the maximum radial compressive stress reaches
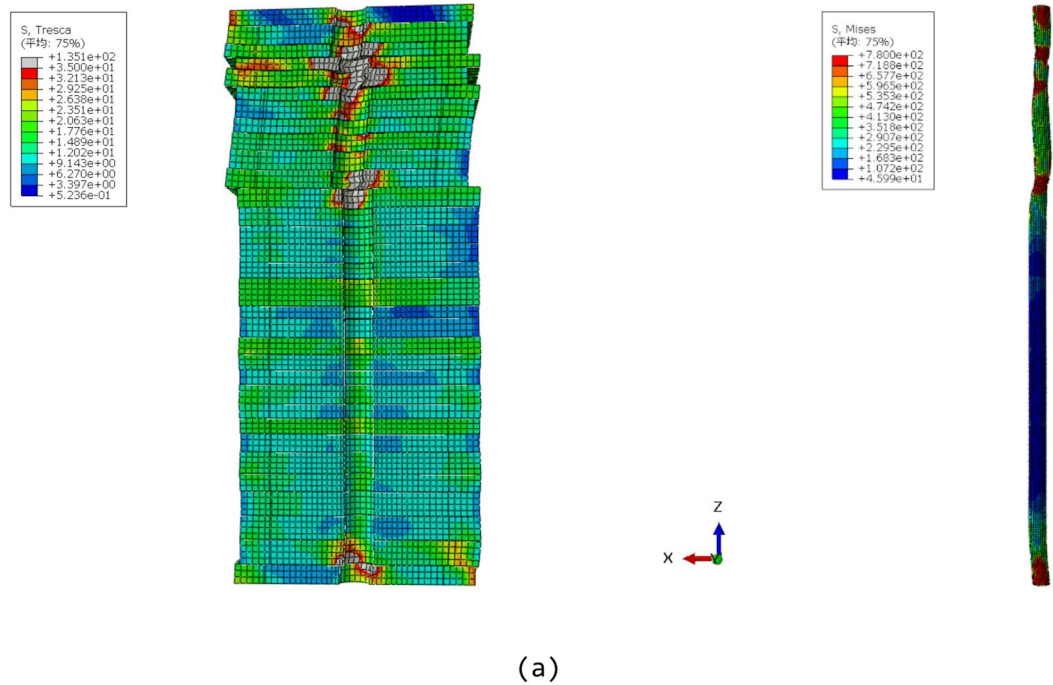
(a)
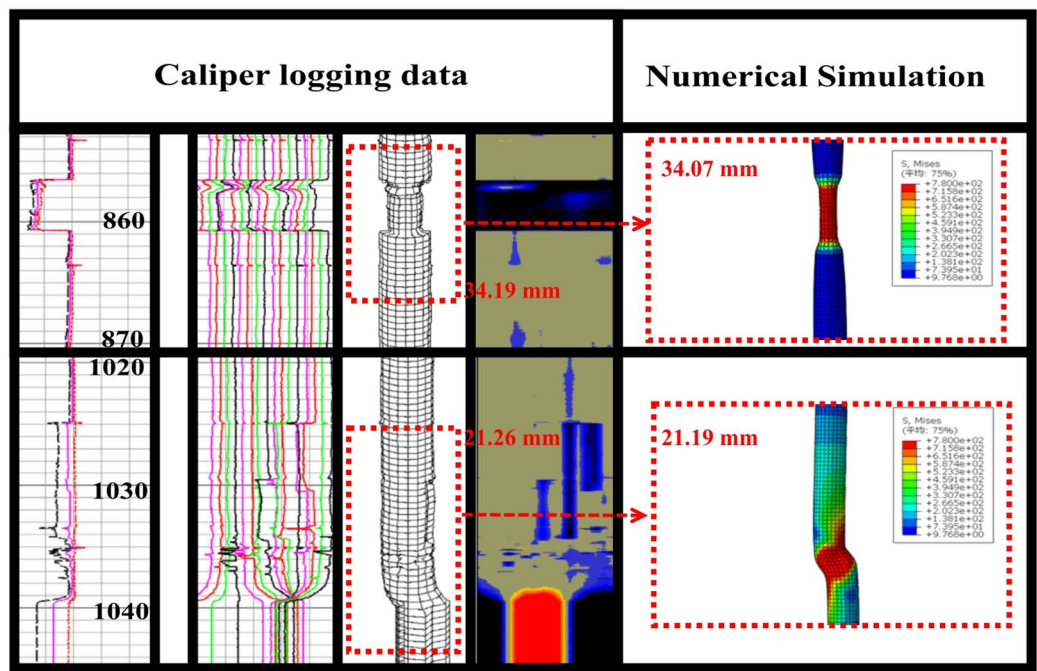
(b)

Fig. 6. Rock mass Tresca stress nephogram and casing Mises stress nephogram. (**a**) Rock mass Tresca stress nephogram and casing Mises stress nephogram. (**b**) Comparison between logging data and numerical simulation of casing deformation.

44.528 MPa, and the maximum radial tensile stress reaches 28.465 MPa. Figure 13 shows the comparison between the finite element circumferential stress and the theoretical collapse strength of the casing with cement sheath according to Eq. (4), at the positions of -100 mm, -50 mm, 0 mm, 50 mm and 100 mm from the sliding center The difference is -19.47%, -7.53%, 5.58%, -8.96%, -23.25% respectively. It can be seen that at a position closer to the sliding center, it is feasible to use the theoretical collapse strength of cement-containing casing to predict.
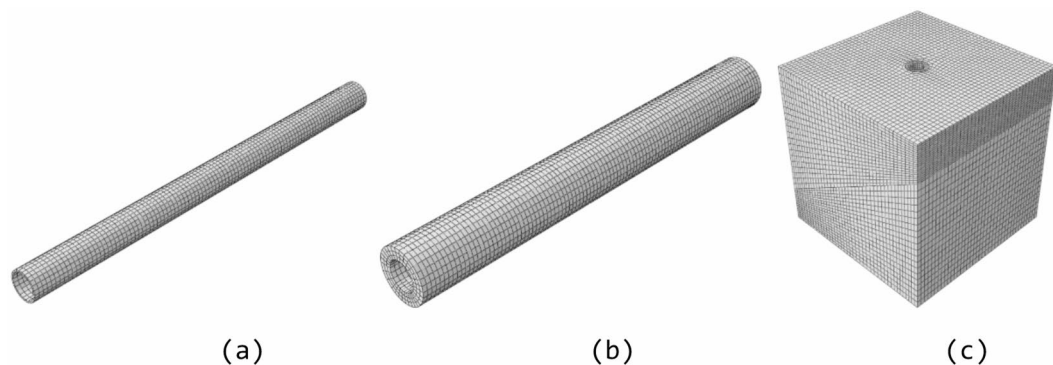
Fig. 7. Schematic diagram of fault slip model. (**a**) Casing. (**b**) Cement. (**c**) Formation.

Part	Number of units	Unit type
Fault hanging wall	31,380	C3D8R
Fault footwall	31,620	C3D8R
Cement sheath	9000	C3D8R
Casing	2400	C3D8R

Table 2. Model unit table.

Parameter	Elastic modulus E/GPa	Cohesion force C/MPa	Internal friction angle Ψ/°	Sliding surface friction coefficient μ
Variation range	2.749–4.749	20–100%C	40–100%Ψ	0.1–0.7

Table 3. Working condition setting.
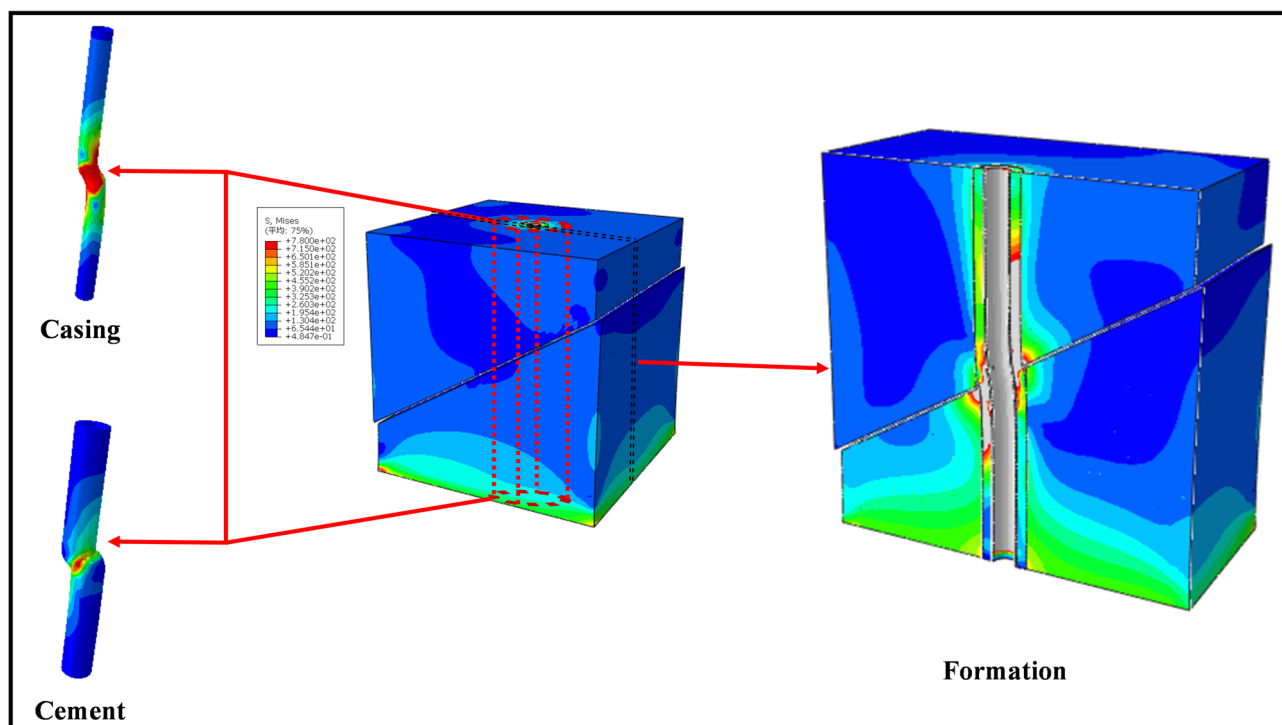
Fig. 8. The model calculation results.

(a)

(b)
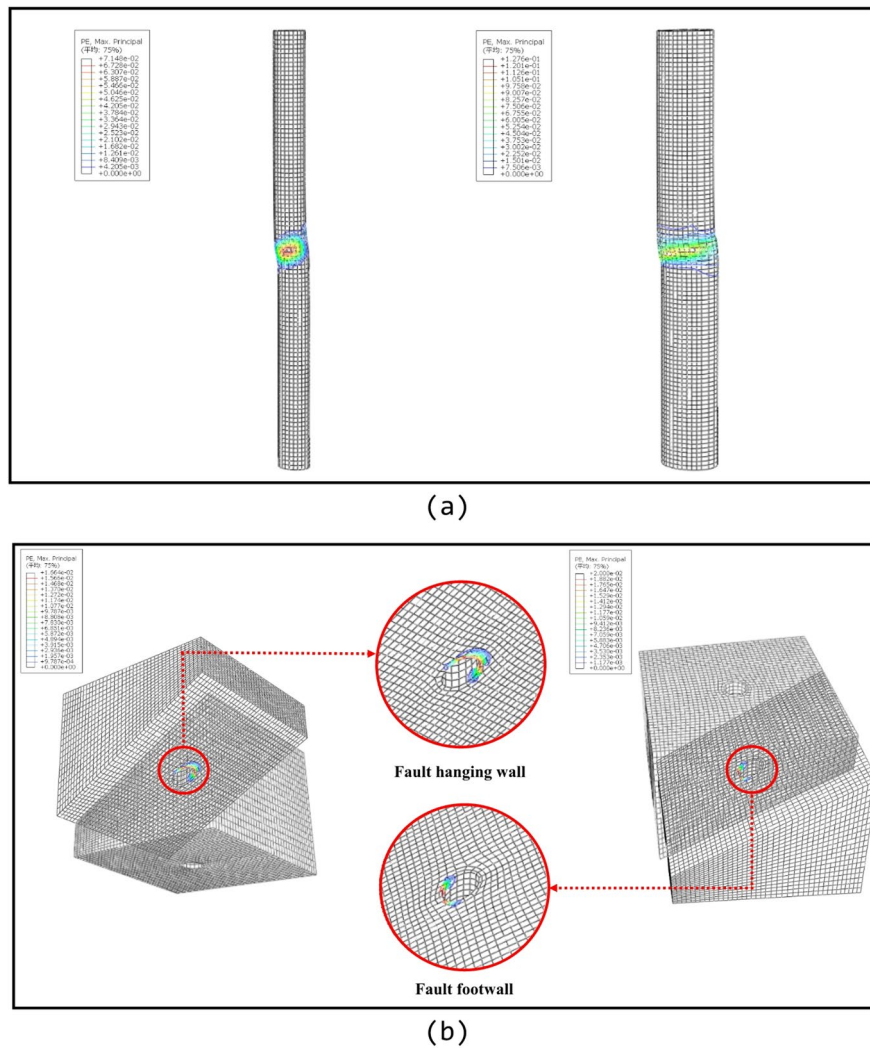
Fig. 9. The plastic zone distribution of the model. (**a**) Distribution of plastic zone of casing and cement sheath. (**b**) Distribution of plastic zones in the hanging wall and footwall of the fault.
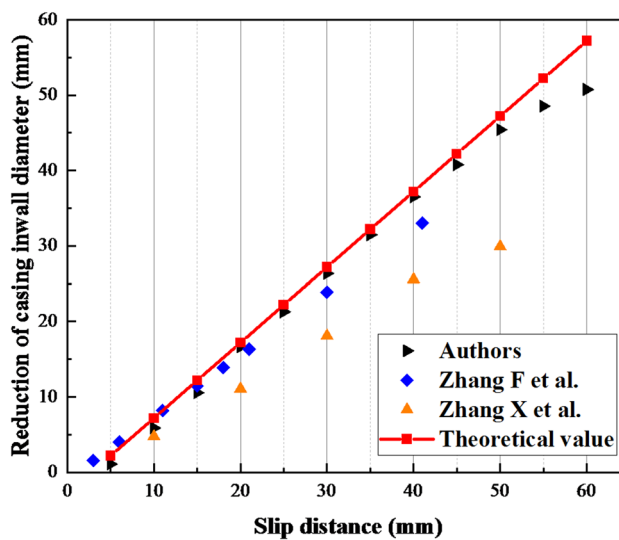
**Fig. 10**. Casing deformation under different sliding distance.

(a)

(b)
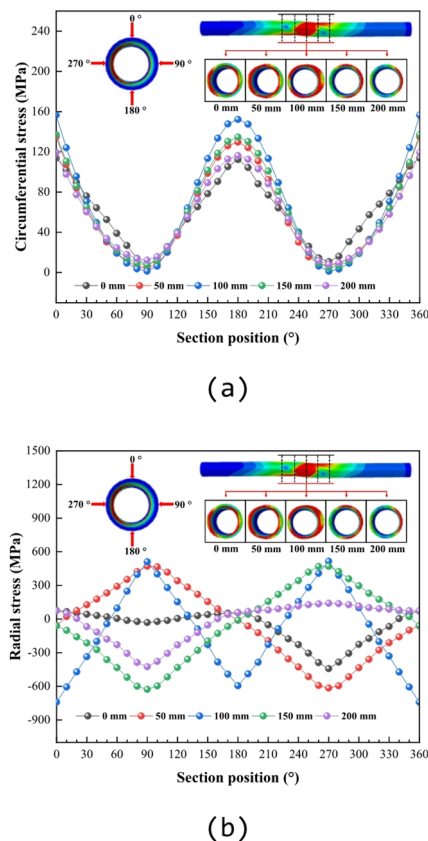
Fig. 11. The stress distribution of the casing at the shear positio. (**a**) The circumferential stress distribution of the casing at shear position. (**b**) The Radial stress distribution of the casing at the shear position.

Influence of reduced rock-strength on fault-slip-type CCFS system damage
Influence of rock mass deterioration on casing

During the fracturing process, the fracturing fluid is immersed into the rock mass. Ai[37] has proved through experiments that the cohesion and the internal friction angle will decrease after the rock is immersed in water. In this part, the effects of cohesion and internal friction angle reduction of rock mass under different elastic modulus and Poisson's ratio on the stress and deformation characteristics of casing are studied.

The test results of the reduction of cohesion of rock masses with different elastic modulus and Poisson's ratio are shown in Figs. 14 and 15. Rock masses with elastic modulus of 4.749 GPA, 3.749 GPA, 2.749 GPA and Poisson's ratio of 0.1, 0.2 and 0.3 are selected for simulation from cohesion not reduced to 80% reduction respectively. The results show that the decrease of cohesion of rock mass will increase the Mises stress and deformation of casing. When the elastic modulus is 2.749 GPA, the casing Mises stress value increases by 4.54 times and the deformation increases by 26.34% when the cohesion is reduced by 80% compared with the case without reduction; When the elastic modulus is 3.749 GPA, the casing Mises stress value increases by 4.35 times and the deformation increases by 19.63% when the cohesion is reduced by 80% compared with the case without reduction; When the elastic modulus is 4.749 GPA, the casing Mises stress value increases by 4.13 times and the deformation increases by 13.82% when the cohesion is reduced by 80% compared with the case without reduction. When Poisson's ratio is 0.1, the casing Mises stress value increases by 24.8% and the deformation increases by 14.27% when the cohesion is reduced by 80% compared with the case without reduction; When Poisson's ratio is 0.2, the casing Mises stress value increases by 25.15% and the deformation increases by 13.05% when the cohesion is reduced by 80% compared with the case without reduction; When Poisson's ratio is 0.3, the casing Mises stress value increases by 30.42% and the deformation increases by 12.82% when the cohesion is reduced by 80% compared with the case without reduction.

Figures 16 and 17 show the test results of the reduction of the internal friction angle in rocks with different elastic modulus and Poisson's ratio. Rock masses with elastic modulus of 4.749 GPA, 3.749 GPA, 2.749 GPA and Poisson's ratio of 0.1, 0.2 and 0.3 are simulated from the internal friction angle not reduced to 60% respectively. The results show that the reduction of internal friction angle of rock mass will increase the Mises stress and deformation of casing. When the elastic modulus is 2.749 GPA, the Mises stress value of casing increases by 24.14% and the deformation increases by 24.55% when the internal friction angle is reduced by 60% compared with the case without reduction; When the elastic modulus is 3.749 GPA, the Mises stress value of casing increases by 23.43% and the deformation increases by 17.95% when the internal friction angle is reduced by 60% compared with the case without reduction; When the elastic modulus is 4.749 GPA, the Mises stress value of the
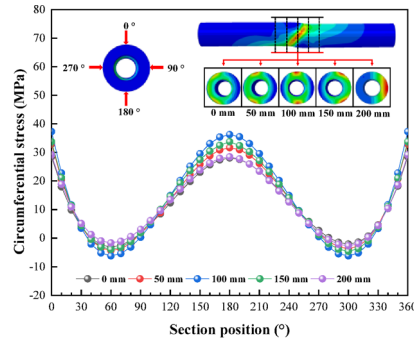
(a)
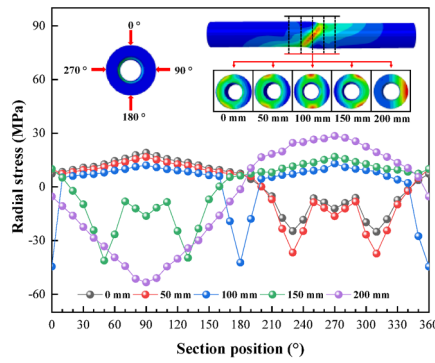
(b)

Fig. 12. The stress distribution of the cement sheath at shear position. (**a**) The circumferential stress distribution of the cement sheath at shear position. (**b**) The radial stress distribution of the cement sheath at shear position.
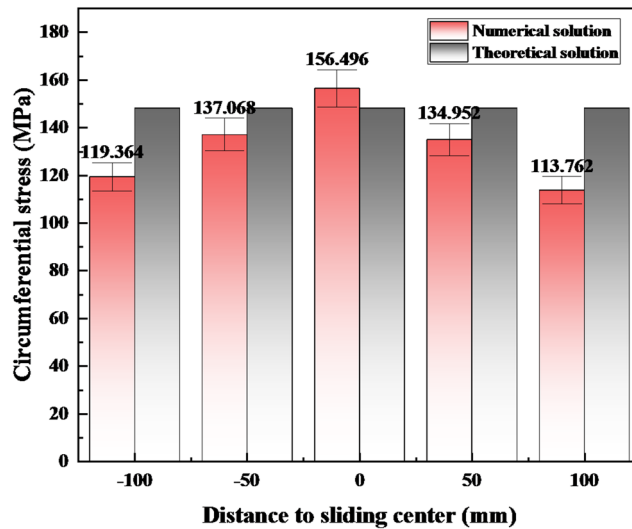

Fig. 13. Comparison between theoretical collapse strength of casing with cement sheath and circumferential stress of finite element model.
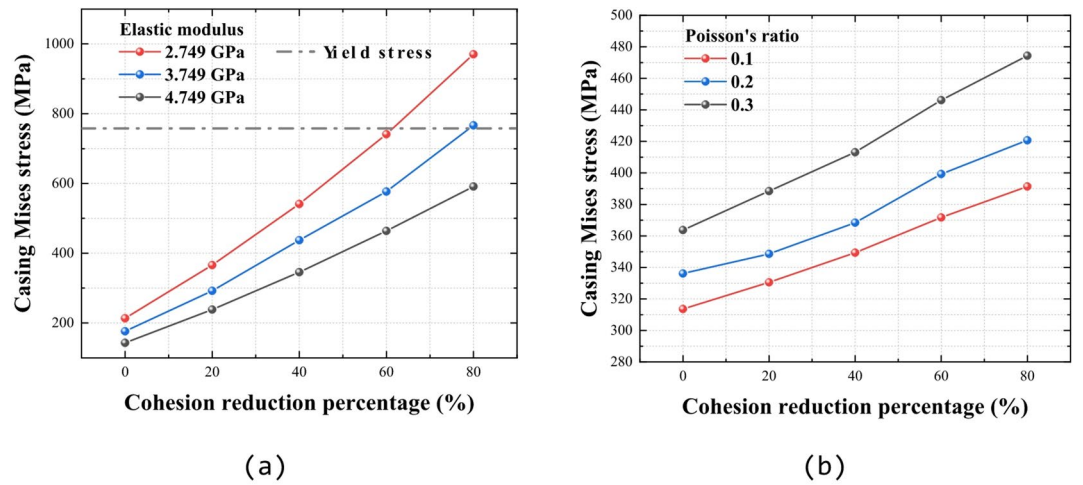
(a)

(b)

Fig. 14. Influence of rock cohesion on casing Mises stress under different elastic modulus and Poisson's ratio. (**a**) Influence of rock cohesion reduction on casing Mises stress under different elastic modulus. (**b**) Influence of rock cohesion reduction on casing Mises stress under different Poisson's ratios.

(a)

(b)
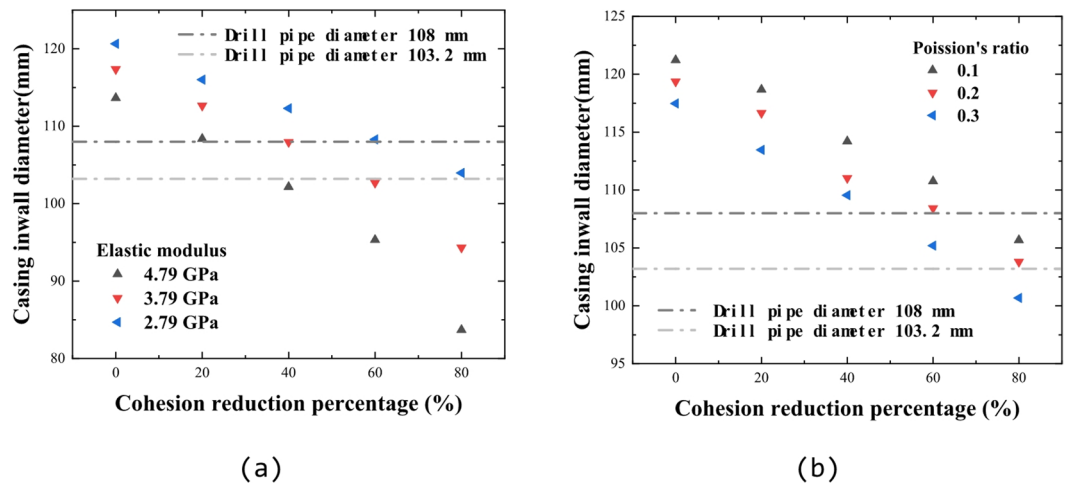
Fig. 15. Influence of rock cohesion on casing inner diameter under different elastic modulus and Poisson's ratio. (**a**) Influence of rock cohesion on casing inner diameter under different elastic modulus. (**b**) Influence of rock cohesion on casing inner diameter under different Poisson's ratio.

casing increases by 22.84% and the deformation increases by 14.47% when the internal friction angle is reduced by 60% compared with the case without reduction. When Poisson's ratio is 0.1, the Mises stress value of casing increases by 46.4% and the deformation increases by 11.86% when the internal friction angle is reduced by 60% compared with the case without reduction; When Poisson's ratio is 0.2, the Mises stress value of casing increases by 48.98% and the deformation increases by 9.56% when the internal friction angle is reduced by 60% compared with the case without reduction; When Poisson's ratio is 0.3, the Mises stress value of casing increases by 49.35% and the deformation increases by 8.68% when the internal friction angle is reduced by 60% compared with the case without reduction.

The results show that the decrease of elastic modulus of rock mass will significantly increase the Mises stress and deformation of casing. Although Poisson's ratio has a certain influence on the stress and deformation, compared with the elastic modulus, the influence is not significant; With the increase of cohesion and the reduction of internal friction angle, the influence of the change of elastic modulus on the stress and deformation of casing gradually increases, and the influence of the change of cohesion on the stress of casing is more significant. The above phenomenon may be caused by the deterioration of the rock mass after immersion in water, which greatly reduces the cohesion of the rock mass. Compared with the non deterioration, the ability of the internal consumption and absorption of stress in the rock mass decreases, resulting in the increase of casing stress.
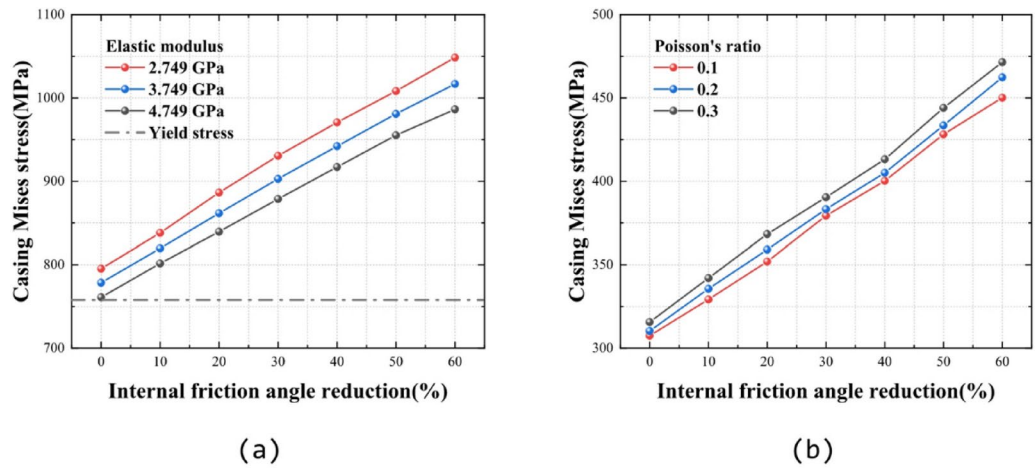
Fig. 16. Influence of friction angle in rock mass on Mises stress of casing under different elastic modulus and Poisson's ratio. (**a**) Influence of friction angle in rock mass on Mises stress of casing under different elastic modulus. (**b**) Influence of friction angle in rock mass on Mises stress of casing under different Poisson's ratio.
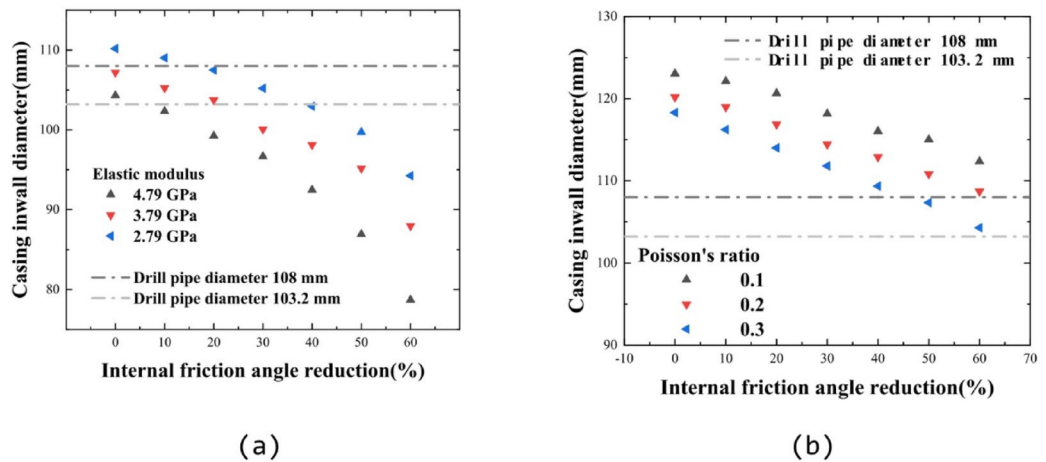

Fig. 17. Influence of friction angle in rock mass on inner diameter of casing under different elastic modulus and Poisson's ratio. (**a**) Influence of rock cohesion on casing inner diameter under different elastic modulus. (**b**) Influence of rock cohesion on casing inner diameter under different Poisson's ratio.

Influence of the change of the friction coefficient of the fault sliding surface on the casing

Both the mineral composition[38] and water content[39] in the rock will affect the friction coefficient of its surface. In this part, the force and deformation of casing under the condition of 60 mm slippage with the original friction coefficient of 0.7 were studied, and the Mises stress and inner diameter changes of casing when the friction coefficient of the sliding surface was reduced from 0.7 to 0.1 were analyzed.

Figure 18 shows the Mises stress nephogram of the casing under different sliding surface friction coefficients, and Fig. 19 shows the Mises stress change of the casing when the friction coefficient of the fault sliding surface is reduced from 0.7 to 0.1. The results show that the Mises stress of the casing increases gradually with the decrease of the friction coefficient of the sliding surface. When the friction coefficient of the fault plane decreases to 0.3, the Mises stress of the casing shear plane increases significantly. When the friction coefficient of the fault plane is 0.7, only the casing near the intersection with the sliding surface (about 80 mm in length) reaches the yield stress. As the friction coefficient of the fault plane decreases, the length of the casing that reaches the yield stress increases. After reducing to 0.1, the length of the casing to reach the yield stress is about 1360 mm, and the Mises stress value reaches 1894.45 MPa, which is 2.49 times the Mises stress value when the friction coefficient of the fault plane is 0.7.

Figure 20 shows the change in the inner diameter of the casing when the friction coefficient of the fault sliding surface is reduced from 0.7 to 0.1. The drill pipe with a diameter of 108 mm and 103.2 mm are blocked in different degrees. The blocked length of the drill pipe with a diameter of 108 mm increased from 170 to 1490 mm, and the blocked length increased by 8.76 times. The blocked length of the drill pipe with a diameter of 103.2 mm increased from 90 to 1170 mm, and the blocked length increased by 13 times.
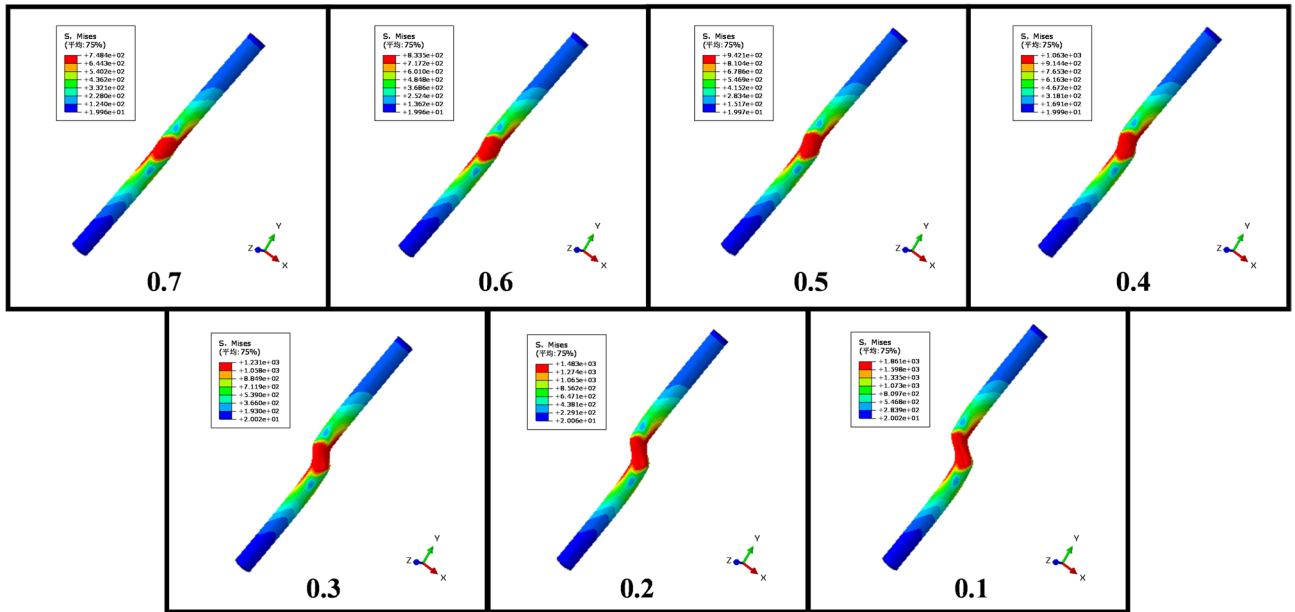
Fig. 18. Mises stress cloud diagram of casing under different sliding surface friction coefficients.
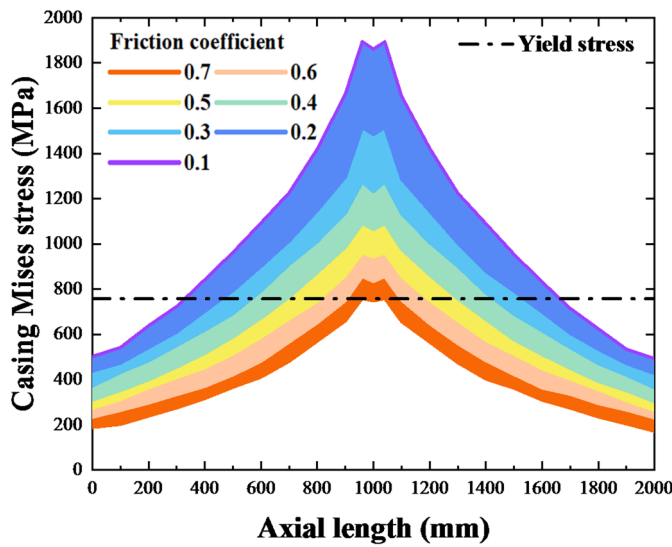

Fig. 19. Variation of Mises stress of casing under different friction coefficients of sliding surfaces.

The results show that the friction coefficient of the sliding surface has an effect on the force and deformation of the casing. When the friction coefficient is greatly reduced, the length of the casing to reach yield and meet resistance increases significantly.

Conclusion

Through the three-dimensional finite element model, the CCFS model under the conditions of the reduction of cohesion and internal friction angle, the reduction of the friction coefficient of the fault plane and the change of the effective stress caused by the water immersion deterioration of the rock mass is studied, and the change of the casing performance after the rock immersion deterioration is analyzed, the result is as follows:

1. The reduction of cohesion and internal friction angle of the rock mass after water immersion will increase the Mises stress and deformation of the casing during the sliding process of the fault, and the reduction of the elastic modulus of the rock mass will also cause the Mises stress and deformation of the casing to decrease, and With the increase of cohesion and the reduction of the angle of internal friction, the influence of the change of elastic modulus on the force and deformation of the casing is gradually enhanced.
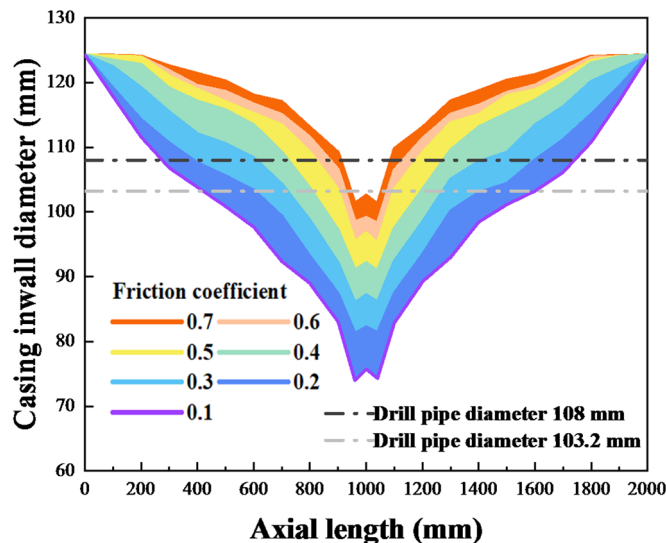
Fig. 20. Variation of casing inner diameter under different friction coefficients of sliding surfaces.

2. The decrease of elastic modulus of rock mass will also cause the Mises stress and deformation of casing to increase significantly. With the increase of cohesion and internal friction angle reduction, the influence of the change of elastic modulus on the stress and deformation of casing will gradually increase. The change of Poisson's ratio of rock mass will have a certain influence on the stress and deformation of casing, but the influence is not significant.

3. The change of the friction coefficient of the fault sliding surface will have a significant impact on the Mises stress and inner diameter deformation of the casing. When the friction coefficient of the fault sliding surface decreases from 0.7 to 0.1, the Mises stress of the casing increases by more than 2 times, and the length of encountering resistance increases 8 times or more.

4. It is recommended to optimize casing steel grades or enhance wall thickness in seismically active or water-sensitive formations to withstand additional stresses caused by rock deterioration, particularly in areas near faults during the fracturing stage. Additionally, precise geological surveys should be conducted before fracturing to accurately locate faults and avoid setting fracturing clusters near low-friction fault zones.

This study systematically analyzes the deformation and stress characteristics of casing under fault slip conditions. It is important to note that the paper only considers the impact of mechanical property degradation of the rock mass due to water saturation on casing deformation and stress, without addressing the effects of fault activation under hydraulic coupling conditions. Investigating the influence of fault activation under hydraulic coupling and its impact on the stability of oil and gas well pipelines will be a focus of our future work.

Data availability

The datasets used and/or analyzed during the current study are available from the corresponding author upon request.

References
1. Cozzi, L. et al. World energy outlook. *Energy* **2020**(2050), 1–461 (2020).
2. Kiran, R. et al. Identification and evaluation of well integrity and causes of failure of well integrity barriers (A review). *J. Nat. Gas. Sci. Eng.* **45**, 511–526 (2017).
3. Mohammed, A. I. et al. Casing structural integrity and failure modes in a range of well types-a review. *J. Nat. Gas. Sci. Eng.* **68**, 102898 (2019).
4. Dutta, J. et al. Production induced faulting risk assessment in a depleted reservoir: A case study from deepwater Krishna-Godavari basin, India. *J. Petrol. Sci. Eng.* **161**, 319–333 (2018).
5. Zoback, M. D. & Gorelick, S. M. Earthquake triggering and large-scale geologic storage of carbon dioxide. *Proc. Natl. Acad. Sci.* **109**(26), 10164–10168 (2012).
6. King, G. E. & Valencia, R. L. Well Integrity for Fracturing and Re-Fracturing: What Is Needed and Why? SPE Hydraulic Fracturing Technology Conference, 2016.
7. Atkinson, C. & Eftaxiopoulos, D. A plane model for the stress field around an inclined, cased and cemented wellbore. *Int. J. Numer. Anal. Meth. Geomech.* **20**(8), 549–569 (1996).
8. Yin, F. & Gao, D. Mechanical analysis and design of casing in directional well under in-situ stresses. *J. Nat. Gas Sci. Eng.* **20**, 285–291 (2014).
9. Fang, J., Wang, Y. & Gao, D. On the collapse resistance of multilayer cemented casing in directional well under anisotropic formation. *J. Nat. Gas Sci. Eng.* **26**, 409–418 (2015).
10. Gao, D., Sun, L. & Lian, J. Prediction of casing wear in extended-reach drilling. *Pet. Sci.* **7**(4), 494–501 (2010).

11. Tan, L., Gao, D. & Zhou, J. Casing wear prediction with considering initial internal casing eccentricity. *Arab. J. Sci. Eng.* **43**(5), 2593–2603 (2018).

12. Li, Z. et al. The influence of shale swelling on casing deformation during hydraulic fracturing. *J. Petrol. Sci. Eng.* **205**, 108844 (2021).

13. Zhao, C. et al. Analysis of the influence of cement sheath failure on sustained casing pressure in shale gas wells. *J. Nat. Gas Sci. Eng.* **66**, 244–254 (2019).

14. Liang, S. et al. Dynamic impacts on the survivability of shale gas wells piercing longwall panels. *J. Nat. Gas Sci. Eng.* **26**, 1130–1147 (2015).

15. Liang, S. et al. Topographic influence on stability for gas wells penetrating longwall mining areas. *Int. J. Coal Geol.* **132**, 23–36 (2014).

16. Yin, F. et al. Casing deformation from fracture slip in hydraulic fracturing. *J. Petrol. Sci. Eng.* **166**, 235–241 (2018).

17. Yin, F. et al. Mechanical behavior of casing crossing slip formation in waterflooding oilfields. *J. Petrol. Sci. Eng.* **167**, 796–802 (2018).

18. Zhang, X. et al. Research on casing deformation mechanism and prevention measures based on micro-seismic signal distribution. *J. Petrol. Sci. Eng.* **217**, 110874 (2022).

19. Yan, X. et al. A new investigation on casing shear deformation during multistage fracturing in shale gas wells based on microseism data and calliper surveys. *J. Petrol. Sci. Eng.* **180**, 1034–1045 (2019).

20. Li, Y., Fukuyama, E. & Yoshimitsu, N. Comprehensive 3-D modeling of mining-induced fault slip: impact of panel length, panel orientation and far-field stress orientation. *Rock Mech. Rock Eng.* **58**(6), 5961–5979 (2025).

21. Li, Y. Spatial distribution of strain energy changes due to mining-induced fault coseismic slip: insights from a rockburst at the yuejin coal mine, China. *Rock Mech. Rock Eng.* **58**(2), 1693–1706 (2025).

22. Li, Y., Fukuyama, E. & Yoshimitsu, N. Mining-induced fault failure and coseismic slip based on numerical investigation. *Bull. Eng. Geol. Env.* **83**(10), 386 (2024).

23. Meng, H. et al. Numerical investigation of casing shear deformation due to fracture/fault slip during hydraulic fracturing. *Energy Sci. Eng.* **8**(10), 3588–3601 (2020).

24. Xi, Y. et al. Research on the influence of strike-slip fault slippage on production casing and control methods and engineering application during multistage fracturing in deep shale gas wells. *Energy Rep.* **7**, 2989–2998 (2021).

25. Feng, Y., Podnos, E. & Gray, K. Well integrity analysis: 3D numerical modeling of cement interface debonding. 50th US rock mechanics/geomechanics symposium, 2016.

26. Feng, Y. et al. Finite-element studies of hoop-stress enhancement for wellbore strengthening. *SPE Drill. Complet.* **30**(01), 38–51 (2015).

27. Feng, Y., Li, X. & Gray, K. Development of a 3D numerical model for quantifying fluid-driven interface debonding of an injector well. *Int. J. Greenhouse Gas Control* **62**, 76–90 (2017).

28. Feng, Y. & Gray, K. Parameters controlling pressure and fracture behaviors in field injectivity tests: a numerical investigation using coupled flow and geomechanics model. *Comput. Geotech.* **87**, 49–61 (2017).

29. Feng, Y. & Gray, K. A parametric study for wellbore strengthening. *J. Nat. Gas Sci. Eng.* **30**, 350–363 (2016).

30. Feng, Y. & Gray, K. E. A fracture-mechanics-based model for wellbore strengthening applications. *J. Nat. Gas Sci. Eng.* **29**, 392–400 (2016).

31. Moradian, Z., Fathi, A. & Evans, B. Shear reactivation of natural fractures in hydraulic fracturing. 50th US Rock Mechanics/Geomechanics Symposium, 2016.

32. Zhang, F. et al. Fault reactivation and induced seismicity during multistage hydraulic fracturing: Microseismic analysis and geomechanical modeling. *SPE J.* **25**(02), 692–711 (2020).

33. Hanks, T. C. & Kanamori, H. A moment magnitude scale. *J. Geophys. Res.: Solid Earth* **84**(B5), 2348–2350 (1979).

34. Cipolla, C., Maxwell, S., Mack, M. *et al.* A practical guide to interpreting microseismic measurements. North American Unconventional Gas Conference and Exhibition, 2011.

35. Mukuhira, Y. et al. Characteristics of large-magnitude microseismic events recorded during and after stimulation of a geothermal reservoir at Basel. *Switzerland. Geothermics* **45**, 1–17 (2013).

36. Heng, S. et al. Anisotropy of shear strength of shale based on direct shear test. *Chin. J. Rock Mech. Eng.* **33**(05), 874–883 (2014).

37. Ai, C. Mechanism and theoretic models of casing failure and numerical calculation with them. Daqing Petroleum Institute, 2003: 1–25.

38. Zhang, F. et al. The role of mineral composition on the frictional and stability properties of powdered reservoir rocks. *J. Geophys. Res.: Solid Earth* **124**(2), 1480–1497 (2019).

39. Xiu, Z. et al. The effects of dry and wet rock surfaces on shear behavior of the interface between rock and cemented paste backfill. *Powder Technol.* **381**, 324–337 (2021).

Acknowledgements

Author contributions

Y. Z.: Writing—Original Draft, Review & Editing, Investigation, Resources. Y. S.: Methodology, Funding acquisition. D. M.: Formal analysis, Funding acquisition, Conceptualization. B. W.: Supervision, Validation, Software, Data Curation. Y.L.: Validation, Visualization.

Funding

Declarations

Competing interests

The authors declare no competing interests.

Additional information

Supplementary Information The online version contains supplementary material available at https://doi.org/1 0.1038/s41598-025-27074-x.

Correspondence and requests for materials should be addressed to B.W.

Reprints and permissions information is available at www.nature.com/reprints.

Publisher's note Springer Nature remains neutral with regard to jurisdictional claims in published maps and institutional affiliations.